Thin-Walled Structures 184 (2023) 110453

Contents lists available at ScienceDirect

Thin-Walled Structures

journal homepage: www.elsevier.com/locate/tws

Full length article

Auxetic and failure characteristics of composite stacked origami cellular materials under compression

Zhen-Yu Li [a], Xin-Tao Wang [a,*], Li Ma [b], Lin-Zhi Wu [a], Lifeng Wang [c]

[a] Key Laboratory of Advanced Ship Materials and Mechanics, College of Aerospace and Civil Engineering, Harbin Engineering University, Harbin 150001, PR China
[b] Center for Composite Materials, Harbin Institute of Technology, Harbin 150080, PR China
[c] Department of Mechanical Engineering, State University of New York at Stony Brook, Stony Brook, NY 11794, USA

ARTICLE INFO

Keywords:
Carbon fibers
Origami structures
Finite element analysis (FEA)
Energy absorption
Auxetic cellular structure

ABSTRACT

The mechanical properties of cellular materials made by stacking layers of origami sheets could be designed over a wide range due to its rich suite of geometry parameters. However, due to the nature of high-volume fraction of air in the structure, these materials may show low stiffness and low strength. Fiber reinforced composites show both higher specific strength and specific stiffness compared with homogeneous materials such as metals and plastics. It could be expected that both the stiffness and strength of stacked origami structures can be improved by introducing fiber reinforced composites. In this investigation, hot molding process is used to produce composite fiber reinforced stacked origami structures. Composite stacked origami structures with different stacking angles and thickness of origami sheets are designed and fabricated. Finite element simulation and experimental compression tests are carried out to investigate their mechanical properties and auxetic characteristics. The effects of origami sheets thickness and stacking angles on the in-plane and out-of-plane auxetic characteristics of the structure are discussed. Finally, the failure modes of the structures during compression are analyzed, and their energy absorption capacity are compared with other honeycomb materials.

1. Introduction

Origami, as an ancient art form, can be used to create sophisticated three-dimensional (3D) decorations or figures by simple folding without cutting [1]. As early as 2005, Mahadevan and Rica [2] discovered the origami phenomenon of 3D topology during the flowering of the hornbeam leaves. In 2014, the unique structural characteristics and multifunctional application potential of fold structure were revealed [3,4]. Since then, origami structures have attracted much attention in the field of lightweight structure research. The unit cell of origami structures can be described by multiple geometric parameters [5], and the auxetic properties of stacked origami structures during in-plane compression or stretching were also studied through folding kinematics [6]. Origami structures have attracted great interest not only in arts, but also in mathematics, computer science and engineering. In the field of engineering application, origami structures have made some achievements, including space deployable structure [7,8], origami robots [4], medicines [9], architecture and civil engineering [10], lightweight structure design [11–13], energy absorption [1,14], vibration absorption [15], etc. Contrary to closed cell sandwich cores like honeycombs which are prone to moisture accumulation, the continuous channels in origami cores enable efficient moisture removal [16]. They also offer new ways to integrate multiple functionalities e.g. heating, ventilation and air conditioning applications into the sandwich structures [17].

In recent years, many origami structures made of paper and metal have been studied on their mechanical properties [18–22]. Because fiber reinforced plastics (FRPs) composites are very soft before curing and can be folded like paper, FRPs have been introduced into the origami structures to improve their specific strength and stiffness [23]. Heimbs et al. [24,25] compared the performances of aramid and carbon fiber reinforced plastic (CFRP) composites fold core sandwich structures by compression, shear, and high/low velocity impact experiments and numerical simulations. Sun et al. [26] fabricated CFRP chevron origami cores sandwich panels using a hot-press molding method. Based on the energy method, the expressions of the compressive elastic modulus and strength of the structure under compression were derived, and the effect of fiber direction on the mechanical properties of the structure was studied. Deleo et al. [27] designed, fabricated and demonstrated foldable-yet stiff-structures made of CFRP composites. The self-deployability and high compactness of the origami structures as well as their abundant potential applications were demonstrated.

Like most core structures such as lattice structure [28–32], re-entrant honeycombs [33–37] structure and double-arrow structure

* Corresponding author.
E-mail address: wangxintao@hrbeu.edu.cn (X.-T. Wang).

https://doi.org/10.1016/j.tws.2022.110453
Received 3 October 2022; Received in revised form 7 December 2022; Accepted 7 December 2022
Available online xxxx

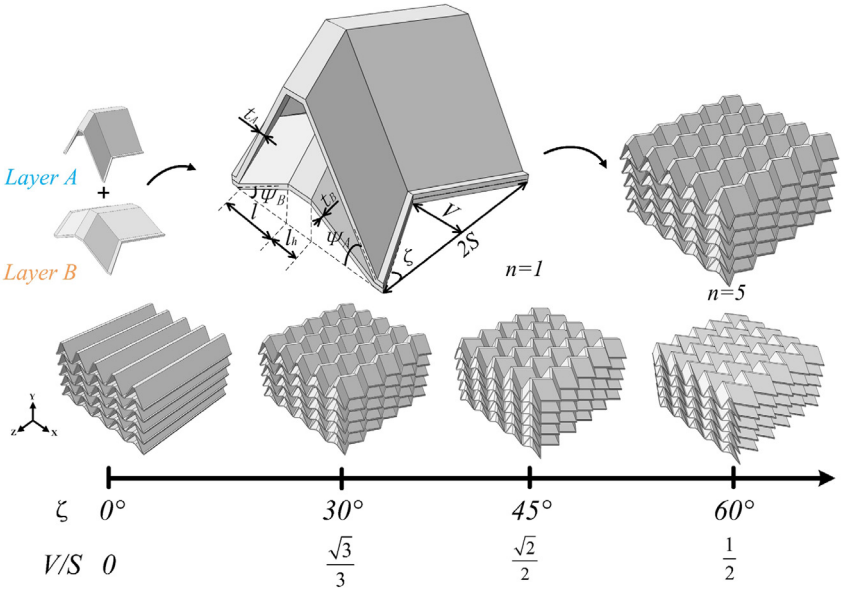

Fig. 1. Geometric parameters of stacked origami structures, and the effect of increasing dimensionless coefficients V/S on structures.

[23,38–40], origami structures can also be stacked by changing certain geometric parameters. Schenk et al. [5] studied two folded metamaterials based on the Miura-Ori fold pattern and found that the mechanics of this metamaterial is mainly determined by the kinematics of folding, independent of its scale. When the structure is compressed in plane, the phenomenon of negative Poisson's ratio appears during the folding process. Harris et al. [41] fabricated metal stacked origami structures use additive manufacturing method. Samples of different cell sizes and cell wall thicknesses were used to perform quasi-static compression tests on the origami samples to evaluate their energy absorption properties and auxetic properties. Harris et al. [14] further measured the dynamic mechanical properties of origami specimens by using an air gun and directly impact Hopkinson bar, and it was observed that the auxetic behavior of the structure decreases under the higher impact velocity due to the local deformation of single fold layer.

It is not difficult to find from previous work of stacked origami structure that when the structure is compressed in different directions, it can produce different degrees of negative Poisson's ratio characteristics. In this paper, the design, fabrication and compression properties of composite stacked origami structures made of high performance CFRP are studied. Section 2 introduces the configuration design and fabrication process of fiber reinforced composite stacked origami structures. Compression experiments are described in Section 3. Finite element simulation is described in Section 4. Comparison of experimental and numerical results, prediction of in-plane and out-of-plane performance with auxetic in all directions, forms of structural failure and comparison with other honeycomb materials are analyzed and discussed in Section 5. Conclusions are drawn in Section 6.

2. Design and manufacturing

Inspired by Schenk and Guest [5], stacked Miura-origami structures shown in Fig. 1 form the basis of the current investigation. This structure has significant advantages due to its rich designable geometric parameters and superior energy absorption performance. The auxetic and energy absorption characteristics of metallic stacked Miura-origami structures had been studied [5,41], while the deformation characteristics and the protective performance of the composite stacked origami structures have not been investigated. Composite stacked origami structures are produced by stacking and bonding origami layers with geometry alternates between successive layers. To improve the bonding strength between adjacent layers, platforms are created on the ridges of each origami layer to increase effective bonding area, as shown in Fig. 1.

2.1. Parametric design of stack structure

The stacked origami structures are characterized by nine geometric parameters shown in Fig. 1: amplitude V, width $2S$, projection length of fold line on XZ plane l, width of the platform at which layer A and layer B is bonded l_h, angles between fold lines and the x-axis Ψ_A and Ψ_B, sheet thickness of layer A (t_A) and layer B (t_B), as well as the number of stacked layers n. Further assuming that layer A and B share the same sheet thickness t, the parameter list is simplified using several sets of dimensionless coefficients: V/S (representing the fold angle ζ) alters the alignment of its facets with z-direction, allowing a smooth transition from a double-arrow honeycomb-like structure (at $V/S = 0$), to a folded structure (as V/S is increased); t/l, represents the sheet thickness, increasing of which means thicken of the sheets; l_h/l, represents the width of the platform, increasing of which means widen of the platform; and $\cos\Psi_A/\cos\Psi_B$ defines the angular combination of the cells in each layer.

The expression for the relative density of the structures can be derived as a function of the dimensionless coefficients mentioned above:

$$\bar{\rho} = \frac{n\frac{t}{l}\sqrt{1+\frac{V^2}{S^2}}\left(\frac{2l_h}{l}\cos\Psi_A + 1 + \frac{\cos\Psi_A}{\cos\Psi_B}\right)}{\left(1+\frac{l_h}{l}\right)\left[n + (1-n)\frac{\cos\Psi_A}{\cos\Psi_B} + 2n\frac{t}{l}\cos\Psi_A\right]} \tag{1}$$

2.2. Specimen geometry and manufacturing

As shown in Fig. 2, composite stacked origami structures are fabricated by a hot molding process. Referring to previous works of Sun et al. and Du et al. [11,26], to prevent prepregs being severely elongated during mold closure, the male molds are designed to be separate strips, as shown in Fig. 2. The molds are made of 7075 aluminum alloy and manufactured using a 4-axis CNC Machine. Carbon fiber reinforced orthogonal plain weave fabrics (LS-3K) with thickness 0.19 mm (Shanghai Lishuo New Material Technology Co. Ltd, PR China) are used to manufacture the origami sheets with different Ψ. Two, three and four layers of the LS-3K prepregs are separately used to produce origami sheets with different thickness. The detailed mechanical property parameters of the composite laminates made from LS-3K prepregs are listed in Table 1 [42]. Before laying the prepreg, the molds are brushed with mold release agent to facilitate the demolding process. The molds are preheated to an appropriate temperature, by

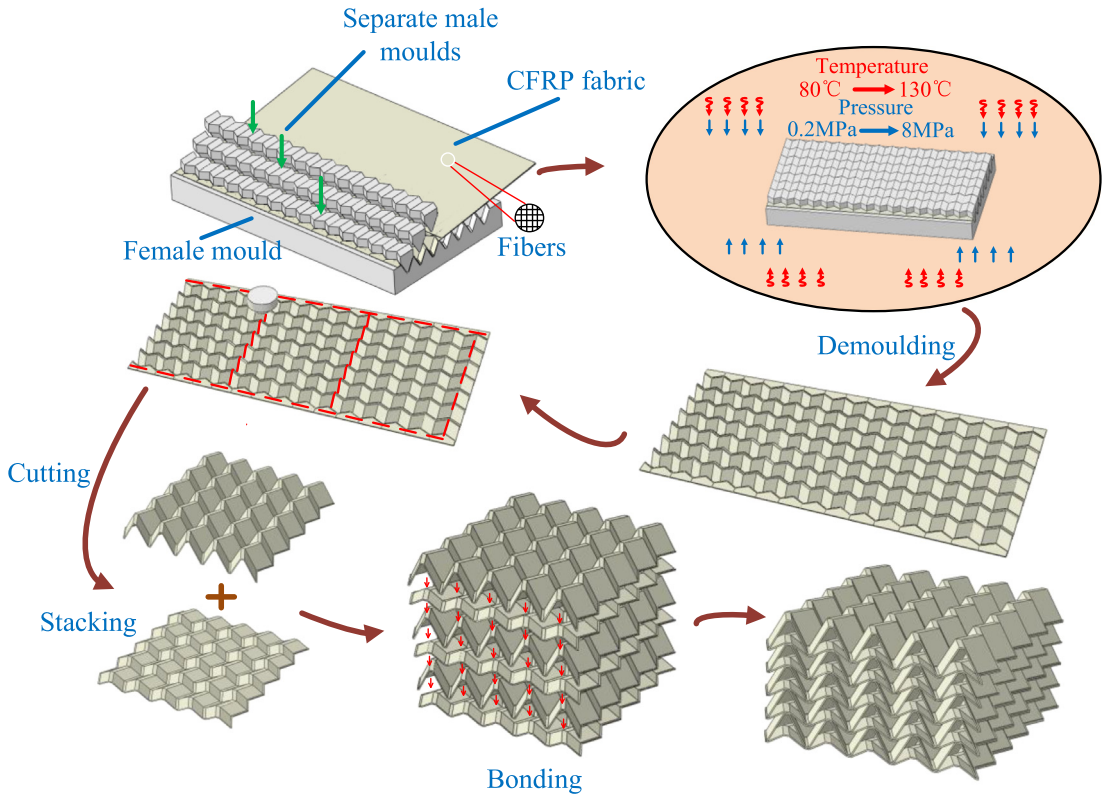

Fig. 2. Fabrication process of CFRP origami stack structures.

Table 1
Mechanical properties of composite laminates (carbon fiber reinforced orthogonal plain weave fabrics (LS-3K)).

Symbol	Value	Property
E_{11}, E_{22}	69 GPa	Longitudinal and transverse Young's modulus
E_{33}	8.3 GPa	Out-of-plane modulus
$\upsilon_{12}, \upsilon_{13}$	0.064	Poisson's ratio
υ_{23}	0.32	Poisson's ratio
G_{12}, G_{13}, G_{23}	4.2 GPa	Shear modulus
X_t, Y_t	756 MPa	Longitudinal and transverse tensile strength
$X_c Y_c$	557 MPa	Longitudinal and transverse compressive strength
Z_t	60 MPa	Out-of-plane tensile strength
Z_c	198 MPa	Out-of-plane compressive strength
S_{12}, S_{13}	118 MPa	Shear strength
S_{23}	86 MPa	Shear strength
ρ	1560 kg/m^3	Density

doing this, the prepregs could absorb heat from the mold and become soft and easy folding during the laying process. The prepregs are fitted into the grooves of the female mold, and then the male molds are singly pressed into the female mold. The assembled molds are then put into the vulcanizing machine to cure the prepregs with a heat-pressing forming process. The curing condition of the prepregs is 80 °C for half an hour under the pressure of 0.2 MPa, and then temperature increases to 130 °C and then held for 1.5 h under the pressure of 8 MPa. After demolding, the carbon fiber reinforced composite origami sheets can be obtained. The composite origami sheets with different Ψ are cut into appropriate size. After that, the composite origami sheets with different Ψ are alternately stacked layer by layer to desired layers number n, and in this paper, n is 5. Double component paste adhesive (J-133C, Heilongjiang Institute of Petrochemical, China) is smeared on the platform to bond the composite origami layers into a composite stacked origami structure. Then, the stacked origami sheets are put into an electrically heated oven to cure the adhesive at 70 °C for 3 h. The final composite stacked origami structures are shown in Fig. 3.

To prepare the composite stacked origami structures, three kinds of molds to produce the composite origami sheets with different Ψ ($\Psi = 60°, 45°, 30°$, respectively) are designed. Two kinds of composite origami sheets with different Ψ create one type of stacked origami structure, thus three types of stacked origami structure are created. Since each composite origami sheet is prepared with three different thickness, nine types of specimens are produced in total. The specimens are named according to the combination of origami sheets with different Ψ and t, as shown in Table 2. For example, 4530-038 indicates that the origami structures are composed of origami sheets with $\Psi_A = 45°$ and $\Psi_B = 30°$, and the thickness of the origami sheets is 0.38 mm. The dimensionless coefficients $V/S = \sqrt{3}/3$ and $l_h/l = 0.25$ are chosen for all specimens, and the relative density of the structure changes with the changing of parameters t/l and $\cos\Psi_A/\cos\Psi_B$, as shown in Eq. (1).

3. Compression tests

It is shown in the work of Harris and McShane [41], the stacked origami structures have better energy absorption performance when

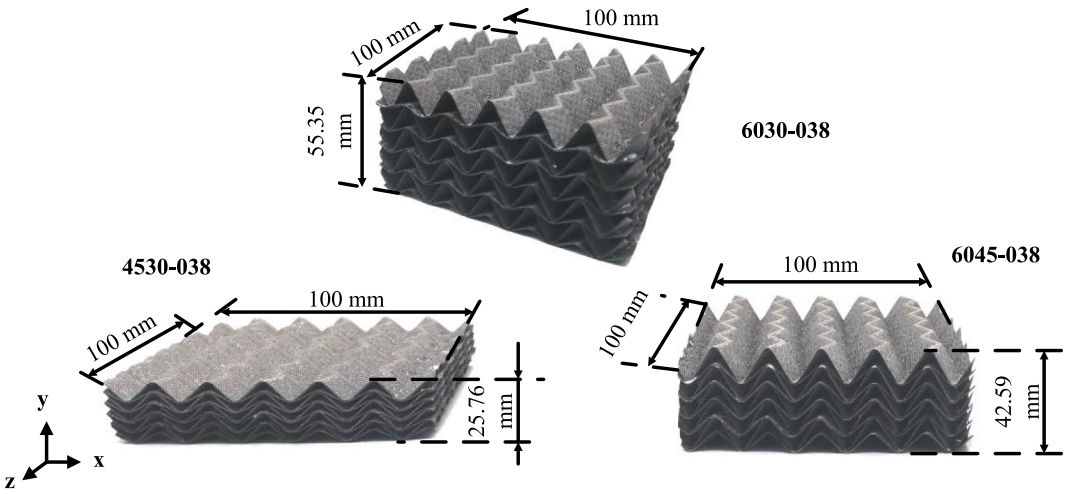

Fig. 3. Specimen images of composite origami stack structures.

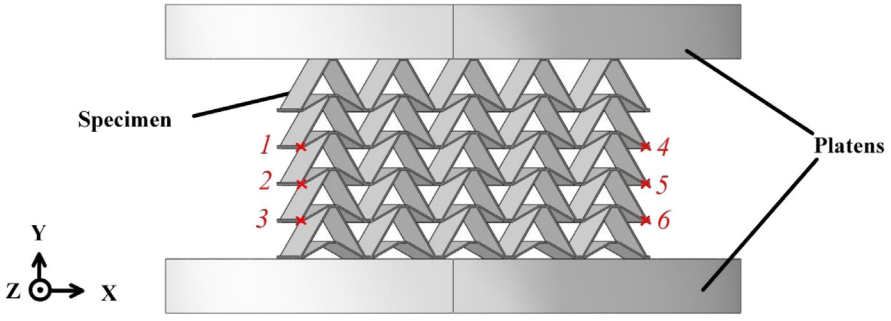

Fig. 4. Schematic diagram of the compressive testing setup.

Table 2
Geometric parameters of nine specimens.

Model	$\overline{\rho}$(%)	t/l	$\frac{\cos\Psi_A}{\cos\Psi_B}$	S (mm)	ζ (°)	t (mm)	l (mm)	l_h (mm)	Ψ_A (°)	Ψ_B (°)
4530–038	18.49	0.0475	0.82	10	30	0.38	8	2	45	30
4530–057	29.68	0.07125	0.82	10	30	0.57	8	2	45	30
4530–076	36.99	0.095	0.82	10	30	0.76	8	2	45	30
6045–038	16.72	0.0475	0.71	10	30	0.38	8	2	60	45
6045–057	23.98	0.07125	0.71	10	30	0.57	8	2	60	45
6045–076	30.61	0.095	0.71	10	30	0.76	8	2	60	45
6030–038	11.75	0.0475	0.58	10	30	0.38	8	2	60	30
6030–057	17.03	0.07125	0.58	10	30	0.57	8	2	60	30
6030–076	21.96	0.095	0.58	10	30	0.76	8	2	60	30

subjected to out-of-plane compression (the load is applied along the y-direction as shown in Fig. 3) compared with the in-plane compression (the load is applied along the x- or z-direction as shown in Fig. 3). Therefore, out-of-plane compression experiments are conducted on the composite stacked origami structures.

The nine types of stacked origami specimens are tested using a universal testing machine Instron 4505 with a 100 kN load cell at a crosshead speed of 2 mm/min (and corresponding strain rate is less than 10^{-3}/s) according to ASTM C365 standard [23]. Two tests are carried out for each type of specimen to ensure repeatability of the results. The experimental setup is shown in Fig. 4. Compressive tests are conducted by putting the specimen between two steel platens, images of the specimens are captured during compression by a digital camera. The displacements history of the gauge points shown in Fig. 4 are traced by analyzing the captured images using GOM Correlate software. The lateral nominal strain of the specimen under compression is calculated referring to the study of Harris and McShane [41]. The distance between node 1 and node 4 is denoted as D_{14}. Similarly, D_{25} and D_{36} are defined. And the relative displacements between these nodes along x-direction during compression are denoted as Δ_{14}, Δ_{25} and Δ_{36}.

The lateral nominal strain ε_x of the specimens are calculated as:

$$\varepsilon_x = \frac{\Delta_{14} + \Delta_{25} + \Delta_{36}}{D_{14} + D_{25} + D_{36}} \tag{2}$$

The nominal compressive strain is defined as:

$$\varepsilon_y = \frac{u}{H} \tag{3}$$

where u is the compressive displacement e.g. the relative displacement between the compression platens, and H is the original height of the specimen.

The Poisson's ratio in the XY plane is defined as:

$$\nu_{yx} = -\frac{\varepsilon_x}{\varepsilon_y} \tag{4}$$

The nominal compressive stress is defined as:

$$\sigma = \frac{F}{A} \tag{5}$$

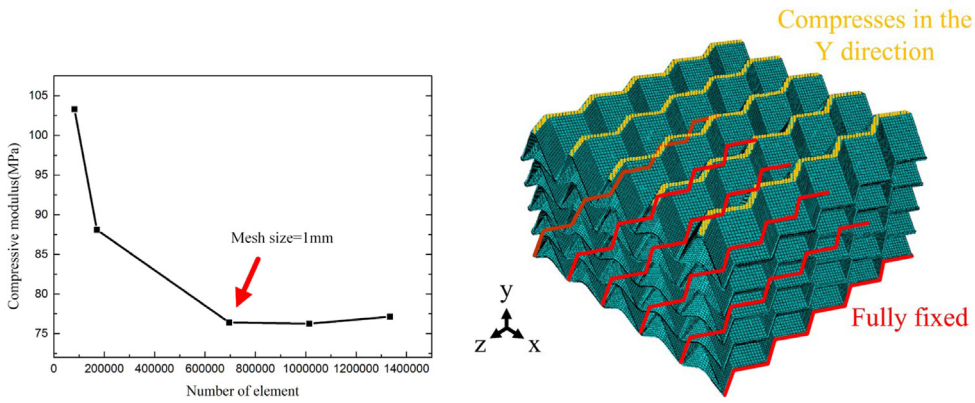

Fig. 5. Mesh sensitivity analysis of "6030-038" and meshing method of origami specimens in simulation.

where F is the compressive force, and it is measured by the load cell of the universal testing machine, and A is the area of the square which bounds the specimen footprint (Fig. 3). This bounding square has side length 100 mm ×100 mm for all the stacked origami specimens.

The effective compression modulus of the structure is defined as:

$$E = \frac{\sigma}{\varepsilon} \tag{6}$$

The (volumetric) energy absorption, W, to a given nominal compressive strain, ε_1, is given by:

$$W\left(\varepsilon_1\right) = \int_0^{\varepsilon_1} \sigma d\varepsilon \tag{7}$$

The contractions of the stacked origami specimens in both lateral directions can be clearly seen during the compression tests, in other words, the specimens display distinct auxetic phenomenon. It is observed that the specimens are damaged layer by layer and the stress–strain curves fluctuate correspondingly. The stress–strain curves increase rapidly when the specimens become condensed under compression. The test results will be discussed in detail in Section 5.

4. Finite element simulations

The Poisson's ratio and failure process of composite stacked origami structures under quasi-static compression are simulated using ABAQUS/Explicit [40]. The FE model for compression tests is depicted in Fig. 5. The stacked origami structure is meshed with eight-node 3D reduced-integration solid elements (designated C3D8R in Abaqus notation). It is shown in Fig. 5 that when the element size drops to 1 mm, the compressive modulus of the model converges, which reflects that element size of 1 mm is fine enough for simulation. The composite sheets are meshed with two elements per ply. In other words, there are 6, 8, 10 elements (corresponding to different thickness) across the thickness of the origami layers sheets. And the mesh of the 6030-038 specimen consists of 696,000 elements comprising a total of 867,188 nodes. Hard contact in the nominal direction and frictionless in the tangent direction are defined between the origami sheets. The adhesive between the bonded layers is not the focus of this study. The bonded layers are merged together in the FE models to avoid vast computational expense. A downward displacement load is exerted on nodes highlighted in yellow in Fig. 5, and all the nodes of the bottom part highlighted in red are fixed.

The vectored user material subroutine (VUMAT) [43] is introduced into the model to simulate the deformation and failure process of the composite stacked origami structures. The modified 3D Hashin's failure criterion and Yeh delaminational failure criteria are used into damage initiation model. In composite laminates, five damage modes can be summarized: fiber tensile fracture, fiber compression fracture, matrix tensile fracture, matrix compression fracture and delamination failure. The corresponding five types of failure modes [43] are defined as:

(a) Fiber stretching ($\varepsilon_{11} > 0$):

$$R_{\mathrm{ft}}^2 = \left(\frac{\varepsilon_{11}}{X_{\mathrm{T}}^{\varepsilon}}\right)^2 + \left(\frac{\varepsilon_{12}}{S_{12}^{\varepsilon}}\right)^2 + \left(\frac{\varepsilon_{13}}{S_{13}^{\varepsilon}}\right)^2 \tag{8}$$

(b) Fiber compression ($\varepsilon_{11} \le 0$):

$$R_{\mathrm{fc}}^2 = \left(\frac{\varepsilon_{11}}{X_{\mathrm{C}}^{\varepsilon}}\right)^2 \tag{9}$$

(c) Matrix tension ($\varepsilon_{22} + \varepsilon_{33} \ge 0$):

$$R_{\mathrm{mt}}^2 = \left(\frac{\varepsilon_{11}+\varepsilon_{33}}{Y_{\mathrm{T}}^{\varepsilon}}\right)^2 + \left(\frac{1}{S_{23}^{\varepsilon}}\right)^2 \left(\varepsilon_{23}^2 - \frac{E_{22}E_{23}}{G_{23}^2}\varepsilon_{22}\varepsilon_{33}\right)^2 + \left(\frac{\varepsilon_{12}}{S_{12}^{\varepsilon}}\right)^2 + \left(\frac{\varepsilon_{13}}{S_{13}^{\varepsilon}}\right)^2 \tag{10}$$

(d) Matrix compression ($\varepsilon_{22} + \varepsilon_{33} < 0$):

$$R_{\mathrm{mc}}^2 = \left(\frac{E_{22}\varepsilon_{22}+E_{33}\varepsilon_{33}}{G_{12}S_{12}^{\varepsilon}}\right)^2 + \left(\frac{\varepsilon_{22}+\varepsilon_{33}}{Y_{\mathrm{C}}^{\varepsilon 2}}\right)\left[\left(\frac{E_{22}Y_{\mathrm{C}}^{\varepsilon}}{2G_{12}S_{12}^{\varepsilon}}\right)^2 - 1\right] + \left(\frac{1}{S_{23}^{\varepsilon}}\right)^2 \left(\varepsilon_{23}^2 - \frac{E_{22}E_{23}}{G_{23}^2}\varepsilon_{22}\varepsilon_{33}\right)^2 + \left(\frac{\varepsilon_{12}}{S_{12}^{\varepsilon}}\right)^2 + \left(\frac{\varepsilon_{13}}{S_{13}^{\varepsilon}}\right)^2 \tag{11}$$

(e) Delamination failure ($\varepsilon_{33} \ge 0$):

$$R_{\mathrm{ld}}^2 = \left(\frac{\varepsilon_{33}}{Z_{\mathrm{T}}^{\varepsilon}}\right)^2 + \left(\frac{\varepsilon_{13}}{S_{13}^{\varepsilon}}\right)^2 + \left(\frac{\varepsilon_{23}}{S_{23}^{\varepsilon}}\right)^2 \tag{12}$$

where $X_{\mathrm{T}}^{\varepsilon}$, $X_{\mathrm{C}}^{\varepsilon}$ are longitudinal tensile and compressive ultimate strain of composite laminates respectively, $Y_{\mathrm{T}}^{\varepsilon}$, $Y_{\mathrm{C}}^{\varepsilon}$ are transverse tensile and compressive ultimate strain respectively, S_{23}^{ε}, S_{12}^{ε} and S_{13}^{ε} are in-plane and out-plane shear ultimate strain respectively, $Z_{\mathrm{T}}^{\varepsilon}$ is tensile delamination ultimate strain. Failure factor R_{i} (i = ft, fc, mt, mc, ld) represents the failure level. These limit strain components are defined as follows:

$$\begin{aligned} &X_{\mathrm{T}}^{\varepsilon} = \frac{X_{\mathrm{T}}}{E_{11}},\ X_{\mathrm{C}}^{\varepsilon} = \frac{X_{\mathrm{C}}}{E_{11}},\ Y_{\mathrm{T}}^{\varepsilon} = \frac{Y_{\mathrm{T}}}{E_{11}},\ Y_{\mathrm{C}}^{\varepsilon} = \frac{Y_{\mathrm{C}}}{E_{22}}, \\ &Z_{\mathrm{T}}^{\varepsilon} = \frac{Z_{\mathrm{T}}}{E_{33}},\ S_{12}^{\varepsilon} = \frac{S_{12}}{G_{12}},\ S_{13}^{\varepsilon} = \frac{S_{13}}{G_{13}},\ S_{23}^{\varepsilon} = \frac{S_{23}}{G_{23}} \end{aligned} \tag{13}$$

The damage variable d_{i} is introduced into the damage evolution process to characterize the damage degree of composites. The definition domain of damage variable d_{i} is [0, 1]. If $d_{\mathrm{i}} = 0$, there is no damage; when $d_{\mathrm{i}} = 1$, the composite material completely lost its mechanical properties. When damage occurs (d_{i}>0), the corresponding mechanical properties (elastic modulus) begin to deteriorate. The relationship d_{i} with R_{i} is shown in Eq. (14):

$$d_{\mathrm{i}} = \begin{cases} 0 & \left(R_{\mathrm{i}} < 1\right) \\ 1 - \frac{1}{R_{\mathrm{i}}^{\mathrm{m}}} & \left(R_{\mathrm{i}} \ge 1\right) \end{cases}, \quad (\mathrm{i} = \mathrm{ft},\ \mathrm{fc},\ \mathrm{mt},\ \mathrm{mc},\ \mathrm{ld}) \tag{14}$$

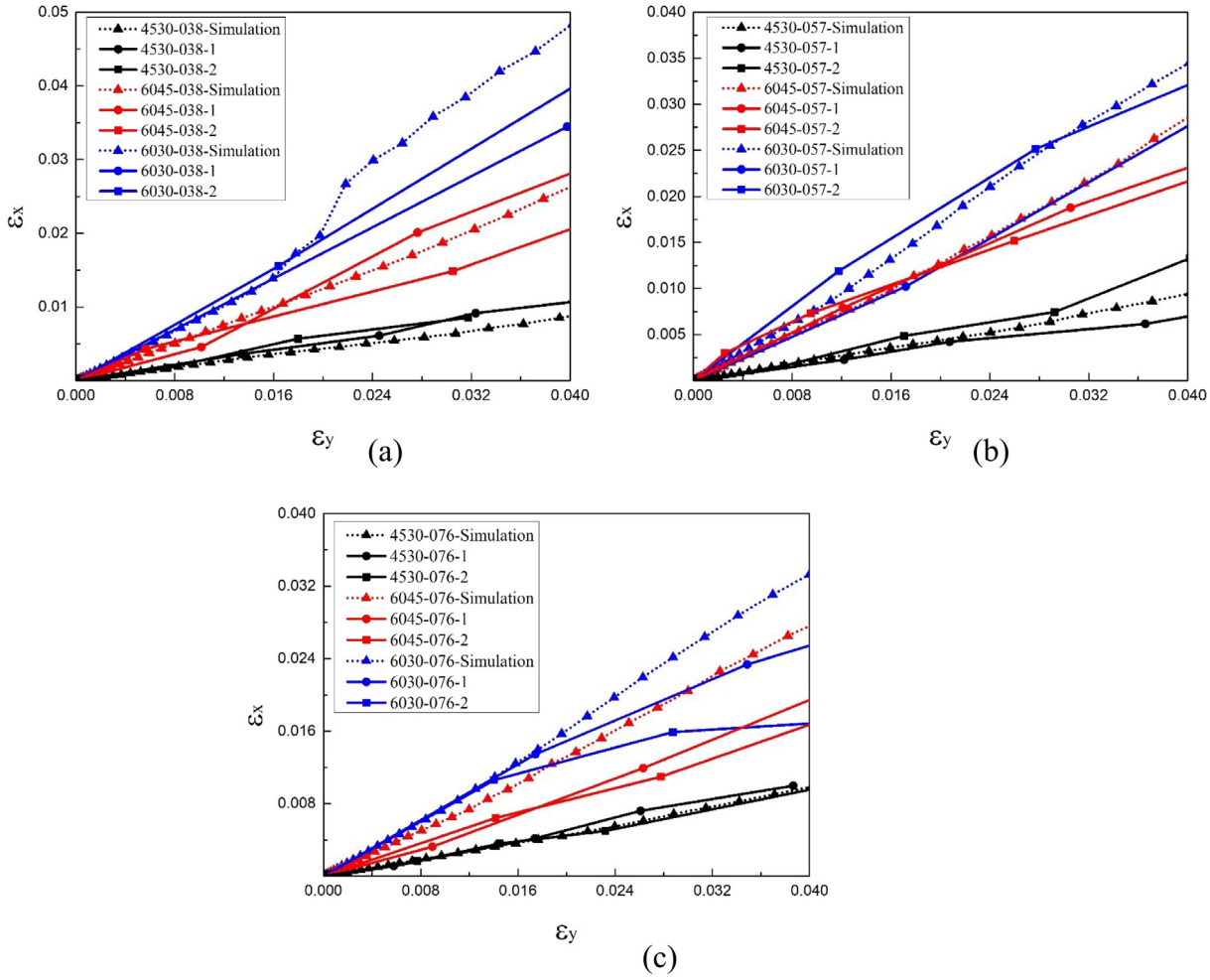

Fig. 6. The comparison between simulation and experimental results of $\varepsilon_x - \varepsilon_y$ curves (the simulation is triangle, test 1 is circle, and test 2 is square).

where m (m>0) is the non-dimensional parameter to control the stiffness degradation rate of composite material [43]. At time t, the damage variable as:

$$d_i^t = max\left(d_i^\tau, 0\right), \quad (\tau \le t; i = ft,\ fc,\ mt,\ mc,\ ld) \tag{15}$$

Based on damage variation, the stress–strain relationship of laminates can be expressed as:

$$\begin{Bmatrix} \epsilon_{11} \\ \epsilon_{22} \\ \epsilon_{33} \\ \gamma_{12} \\ \gamma_{23} \\ \gamma_{13} \end{Bmatrix} = \begin{bmatrix} \frac{1}{E_{11}(1-\omega_1)} & -\frac{\nu_{12}}{E_{22}} & -\frac{\nu_{13}}{E_{33}} & & & \\ -\frac{\nu_{12}}{E_{22}} & \frac{1}{E_{22}(1-\omega_2)} & -\frac{\nu_{23}}{E_{22}} & & 0 & \\ -\frac{\nu_{13}}{E_{33}} & -\frac{\nu_{23}}{E_{22}} & \frac{1}{E_{33}(1-\omega_3)} & & & \\ & & & \frac{1}{G_{12}(1-\omega_4)} & 0 & 0 \\ & 0 & & 0 & \frac{1}{G_{23}(1-\omega_5)} & 0 \\ & & & 0 & 0 & \frac{1}{G_{13}(1-\omega_6)} \end{bmatrix} \times \begin{Bmatrix} \sigma_{11} \\ \sigma_{22} \\ \sigma_{33} \\ \tau_{12} \\ \tau_{23} \\ \tau_{13} \end{Bmatrix} \tag{16}$$

where damage parameter $\omega_i = (i = 1, \ldots, 6)$ is defined as:

$$\begin{aligned} &\omega_1 = max\left(0, d_f\right), \omega_2 = max\left(0, d_f, d_m\right), \omega_3 = max\left(0, d_f, d_d\right), \\ &\omega_4 = max\left(0, d_f, d_m\right), \omega_5 = max\left(0, d_f, d_d\right), \omega_6 = max\left(0, d_f, d_d\right), \\ &d_f = max\left(0, d_{ft}, d_{fc}\right), d_m = max\left(0, d_{mt}, d_{mc}\right), d_d = max\left(0, d_{ld}\right) \end{aligned} \tag{17}$$

According to the failure criterion, the unit stiffness will degenerate when a unit fails. Therefore, the maximum strain criterion is applied in the VUMAT subroutine to remove the distorted elements [43].

5. Results and discussion

5.1. Auxetic behavior

The simulation and experimental results of $\varepsilon_x - \varepsilon_y$ curves are shown in Fig. 6, and the opposite number of the slope represents the Poisson's ratio of the composite stacked origami structures. Poisson's ratios ν_{yx} of all specimens at the stage of small deformation are shown in Fig. 7(a). It can be seen from Fig. 7(a), changing the origami sheets thickness t does not have a distinct influence on the overall Poisson's ratio. The composite origami stack structures with different angle combinations have different Poisson's ratios. In the configuration selected in this paper, the auxetic property of the structure increases with the decrease of $\cos\Psi_A / \cos\Psi_B$, which indicates that when the dimensionless coefficient V/S remains constant, the auxetic property of the structure depends on the different angle combinations of the structure, and the auxetic property of the structure is positively correlated with the overall height of the structure.

It is shown in Fig. 7(a) that the Poisson's ratios of the specimens can be well predicted by simulation. Therefore, FE simulation is used to predict Poisson's ratios of the structures in the following discussion. When the composite stacked origami structures are compressed out-of-plane, the structures display good omnidirectional auxetic behavior, that is,

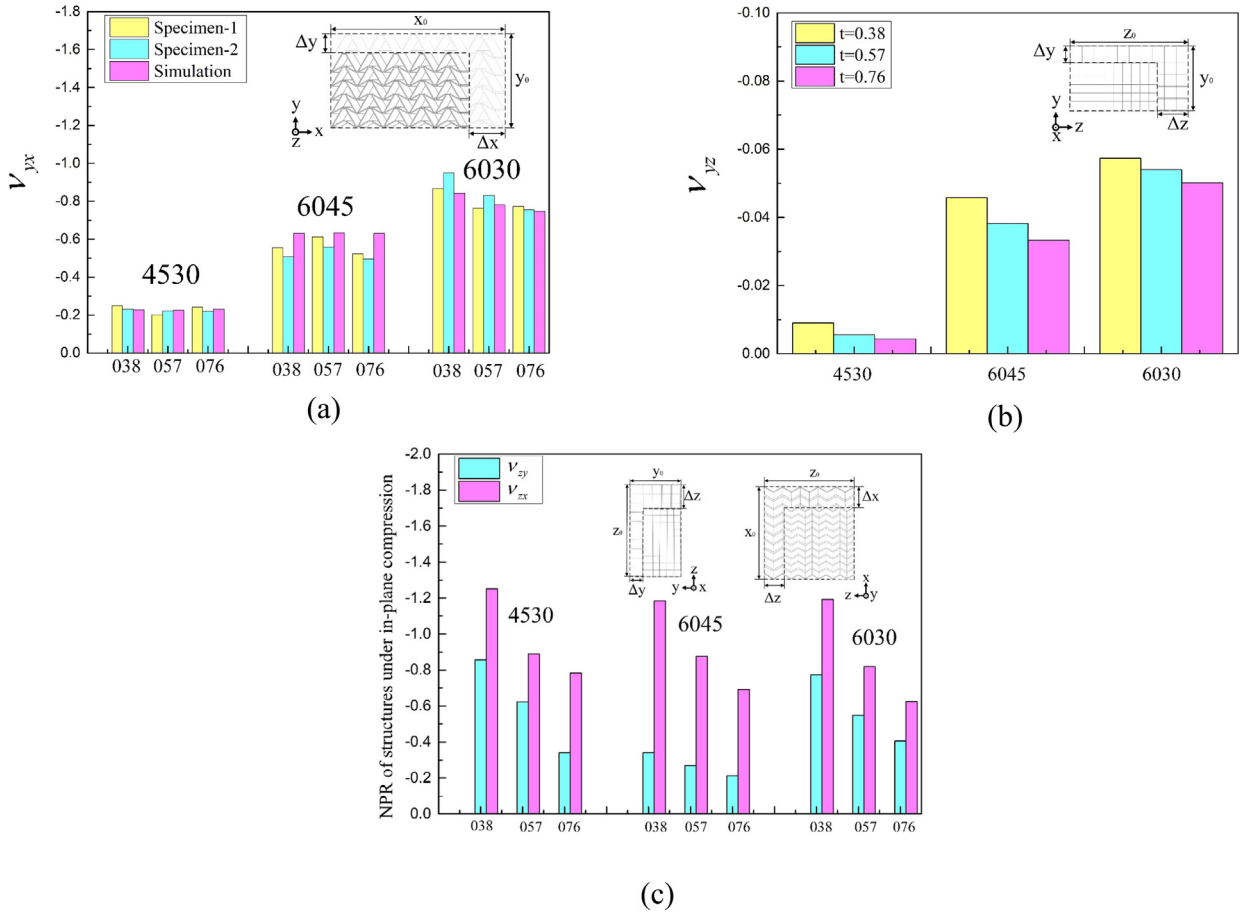

Fig. 7. Auxetic properties of structures under in-plane and out-of-plane compression.

both the XY plane and the YZ plane own good auxetic character. The Poisson's ratios v_{yz} are shown in Fig. 7(b). It is shown in Fig. 7(b) that as the total height of the structure increases ($\cos\Psi_A/\cos\Psi_B$ decreases accordingly), the auxetic property of the structure also increases, which is consistent with the auxetic property of parameter $\cos\Psi_A/\cos\Psi_B$ on the XY plane during out-of-plane compression mentioned above. Under out-of-plane compression, the specimen exhibits the strongest auxetic properties in the XY plane. When compressed in-plane, that is, pressure is applied along the z-direction as shown in Fig. 3, the Poisson's ratios are shown in Fig. 7(c). Different from the out-of-plane compression, in-plane compression has the same size in the height direction (z-direction is 100 mm). It is not difficult to find that the composite stacked origami structures with the same thickness and different angle combinations have very similar v_{zx}, which mainly due to that v_{zx} depends on the parameters V and S [5], while V and S in this paper are fixed. Unlike out-of-plane compression, the origami sheets thickness t has a distinct effect on its auxetic characteristics during in-plane compression. Both v_{zy} and v_{zx} increase (less auxetic) with the increase of the origami sheets thickness t. Existing angle combinations during in-plane compression, structures 6030 and 4530 have similar Poisson's ratio v_{zy}, and their absolute values are higher than those of structure 6045.

5.2. Compressive response, deformation mechanisms and failure modes

Fig. 8 shows the comparison of the experiment results and **FE** results of the stress–strain curves. It is shown that the experiment results and **FE** results match well in trend especially the occurrence and number of stress peaks. While the failure stresses of experiments are significantly lower than **FE** results. And this may be caused by manufacturing defects. The fibers of the composite near the folding lines of the origami layers are adversely stretched during fitting the prepregs into the grooves of the female molds, which causes defects in the specimens. The manufacturing defects lead to the stress difference of experiments and FE. Measures should be taken in the future studies to reduce manufacturing defects to improve the mechanical properties of the composite origami stack structures. By comparing composite stacked origami structures with the same thickness, it can be seen that the compressive stiffnesses (the slopes of stress–strain curves) of structures 6045 and 4530 are similar, and the compressive stiffness of the structure 6030 is lower than that of 6045 and 4530. This is mainly because the 6045 and 4530 structures have similar relative densities, while the relative density of the 6030 structure is lower. Finally, we can also find that structures 6030 and 6045 have similar failure trend.

The comparison of the failure modes between simulation and experiment of the composite stacked origami structures with different angle combinations when the thickness $t = 0.38$ mm is shown in Fig. 9. It can be seen that the failure modes of the structures during compression can be well captured by the finite element simulations.

To study the influences of the parameter t/l on the compressive responses of the specimens, the representative compressive stress–strain responses of the specimens with the same parameter Ψ_A and Ψ_B, but different parameter t/l are plotted in Figs. 10–12. It can be seen from Figs. 10–12 that each type of the composite stacked origami structures undergo three stages of linear elasticity, buckling and crushing. Besides, the slopes of the stress–strain curves of the specimens increase monotonously with increasing origami sheet thicknesses (thus the bending stiffnesses) at the early stage for the specimens. As shown

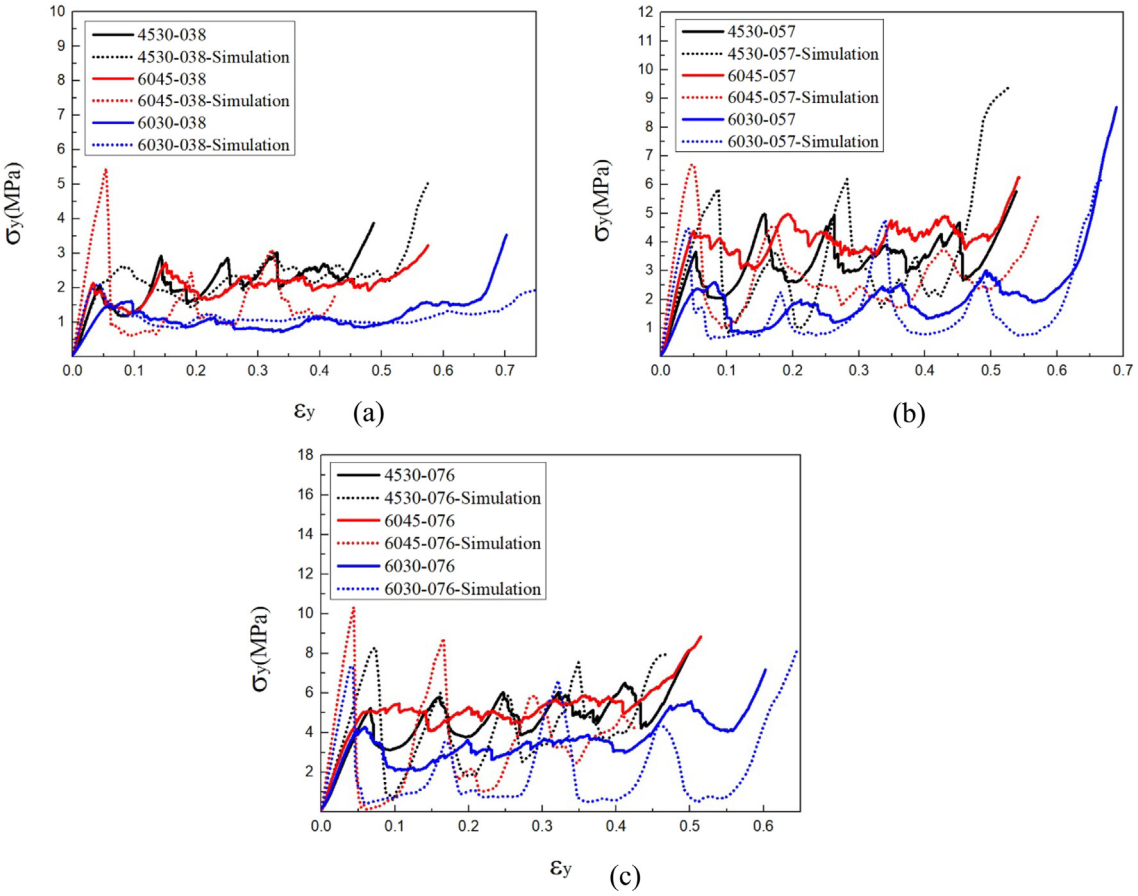

Fig. 8. Simulation and experimental results of the stress–strain curves of different parameter $\cos\Psi_A/\cos\Psi_B$ under the same parameter t/l.

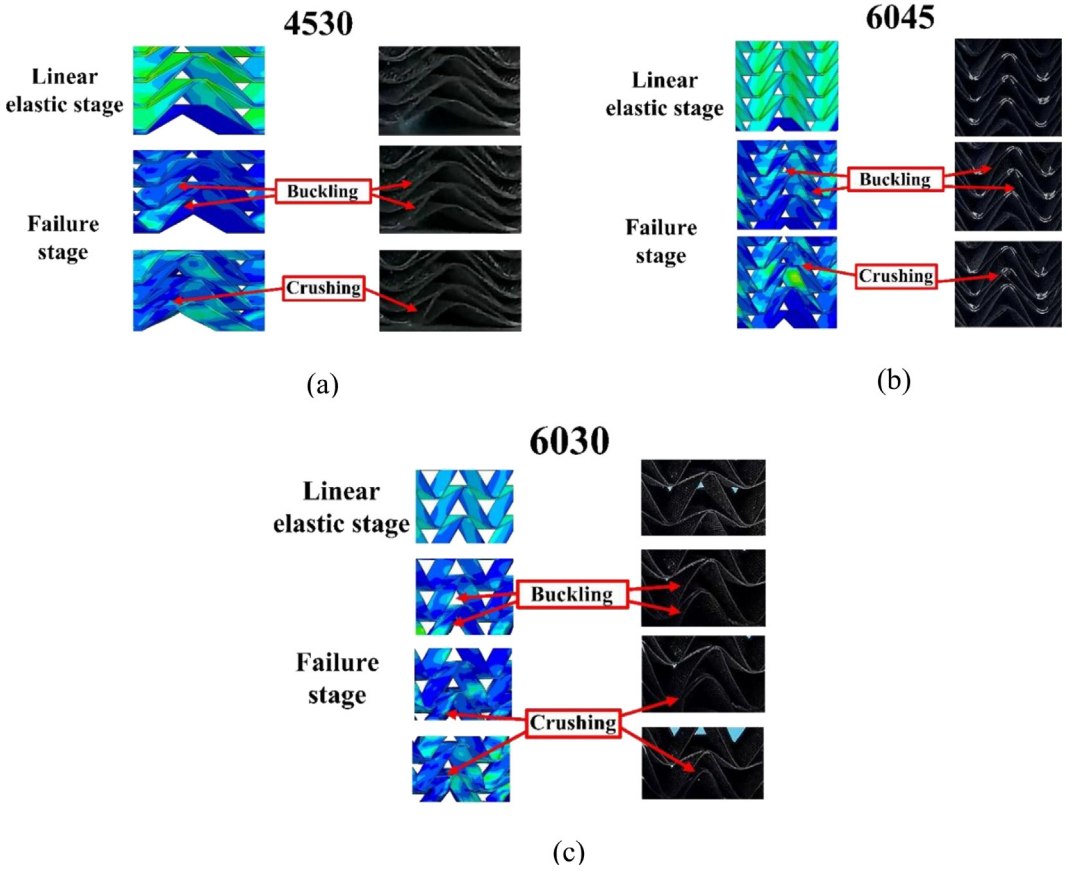

Fig. 9. Simulation and experimental comparison of composite stacked origami structures with thickness $t = 0.38$ mm.

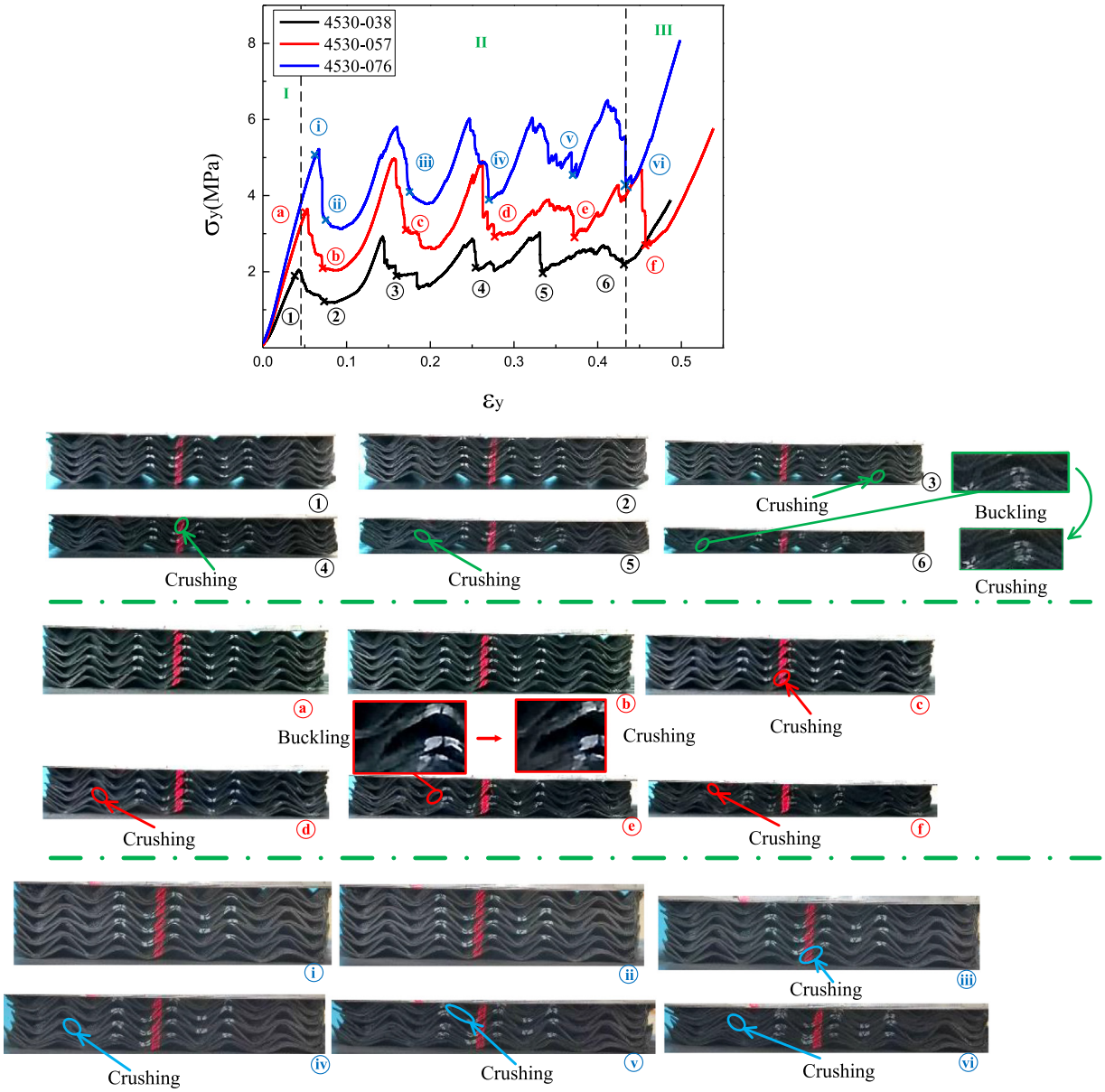

Fig. 10. Failure process of composite origami stack structure with the same parameter $\cos\Psi_A/\cos\Psi_B = 0.82$, and t/l = 0.0475, 0.07125, 0.095, respectively.

in Fig. 10 and Fig. 11, when the thickness reaches a certain value (0.57 mm in this study) and the difference between parameters Ψ_A and Ψ_B is small (15° in this study), the change of equivalent compression modulus (slope of the curve at the linear stage) of composite stacked origami structures are small. However, with the increase of the thickness, the stress peak of the structure increases.

The stress–strain curve of structures 4530 with different t/l can be seen in Fig. 10. Significant states of the specimens during compression are depicted for better illustration of the compression behavior. In the beginning, the stress increases linearly with the applied strain. The cells are compressed elastically (Fig. 10**(1) (a)** and **(i)**) until the destruction of the first layer of specimens. With the obvious increase of the compression displacement, the height of the other four layers of the specimens except the first layer did not decrease significantly. As the parameters $\cos\Psi_A/\cos\Psi_B$ and t/l of the composite stacked origami structures increase, the buckling of the inclined plate is not easily detected during compression (for composite stacked origami structure 4530, the buckling phenomenon is only found in Fig. 10**(6)** and **(e)**). When one layer of composite stacked origami structure is damaged, a transition platform appears on the stress–strain curve with the compaction of the failure layer. When the failure layer compacts, the structure enters the next failure cycle. In the end, when the sheets of the last layer of cells begin to touch each other, densification appears as a steep rise in stress (Fig. 10**(6)**, **(f)** and **(vi)**). It can be seen from the figure that, like other porous structures [6,44,45], the higher the wall thickness (relative density), the earlier the structure densification (the smaller the densification strain). Finally, to clarify the failure process of the composite folding stack structure, the failure process is classified into three stages in the compression process: (I) Linear elastic stage, (II) Plateau in stress stage, and (III) Densification stage.

The sheet of layer A bears compression and bending, and layer B bears tensile and bending. So, buckling always happen in layer A and followed by crushing. Three phases of response also can be observed from Figs. 11 and 12 for the structures of 6045 and 6030. Different from the structure of 4530, with the parameter Ψ_A increase, the buckling phenomenon of the structure before failure becomes obvious due to the

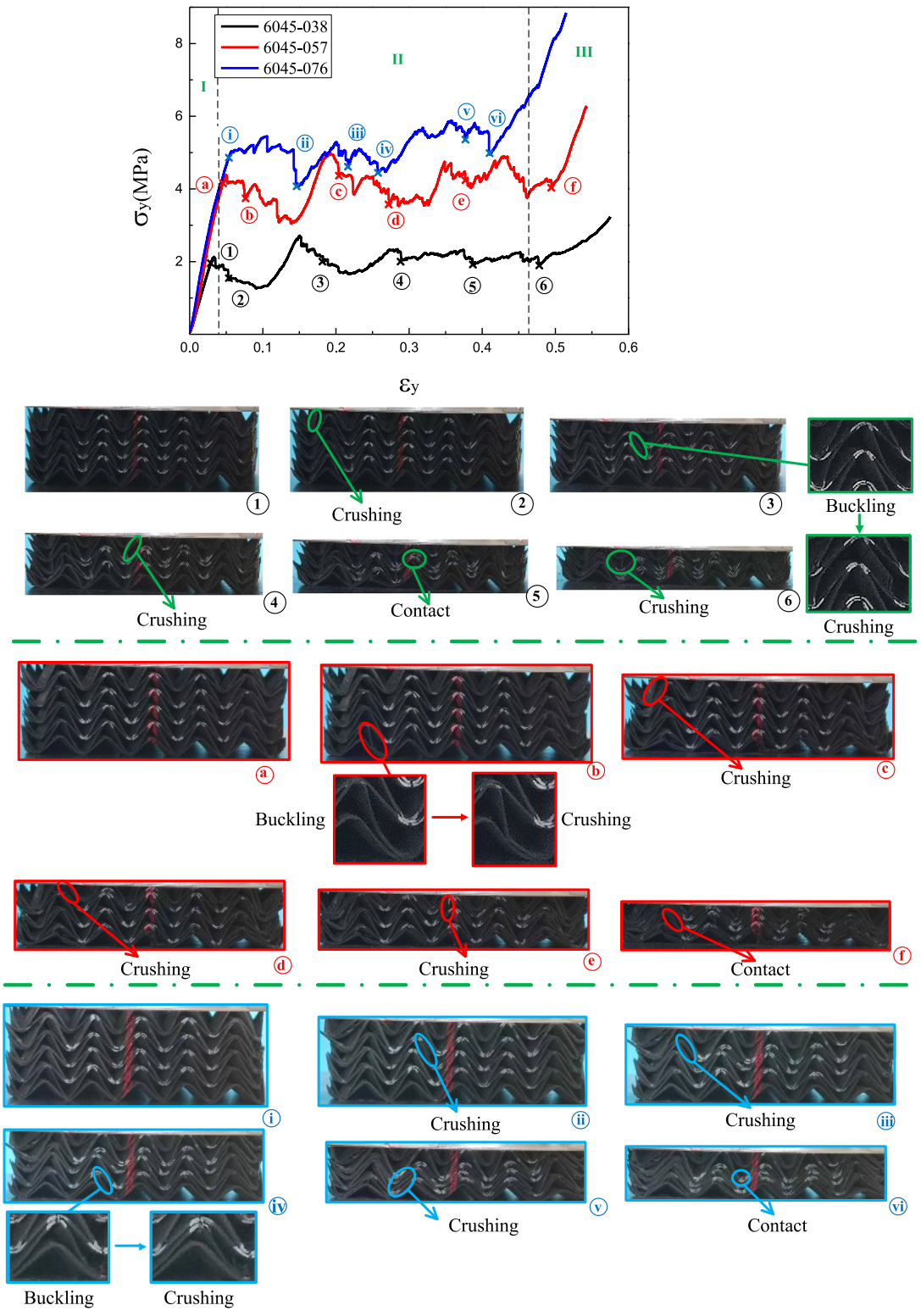

Fig. 11. Failure process of composite origami stack structure with the same parameter $\cos\Psi_A/\cos\Psi_B = 0.71$, and t/l = 0.0475, 0.07125, 0.095, respectively.

increase of the length to thickness ratio of facet of layer A, as shown in Figs. 11 and 12.

5.3. Energy absorption capacity

In this section, the compressive stiffness and energy absorption capacity of the composite stacked origami structures of this work are compared with those of other auxetic structures. The compressive modulus is evaluated based on the slope of the linear stage of the stress–strain curve. Energy absorption capacity is calculated based on Eq. (7), and the minimum strain is zero and the maximum strain is compaction strain. As shown in Fig. 13**(a)**, the compressive stiffness of the composite stacked origami structures in this work is compared with the auxetic structure prepared by different processes by referring

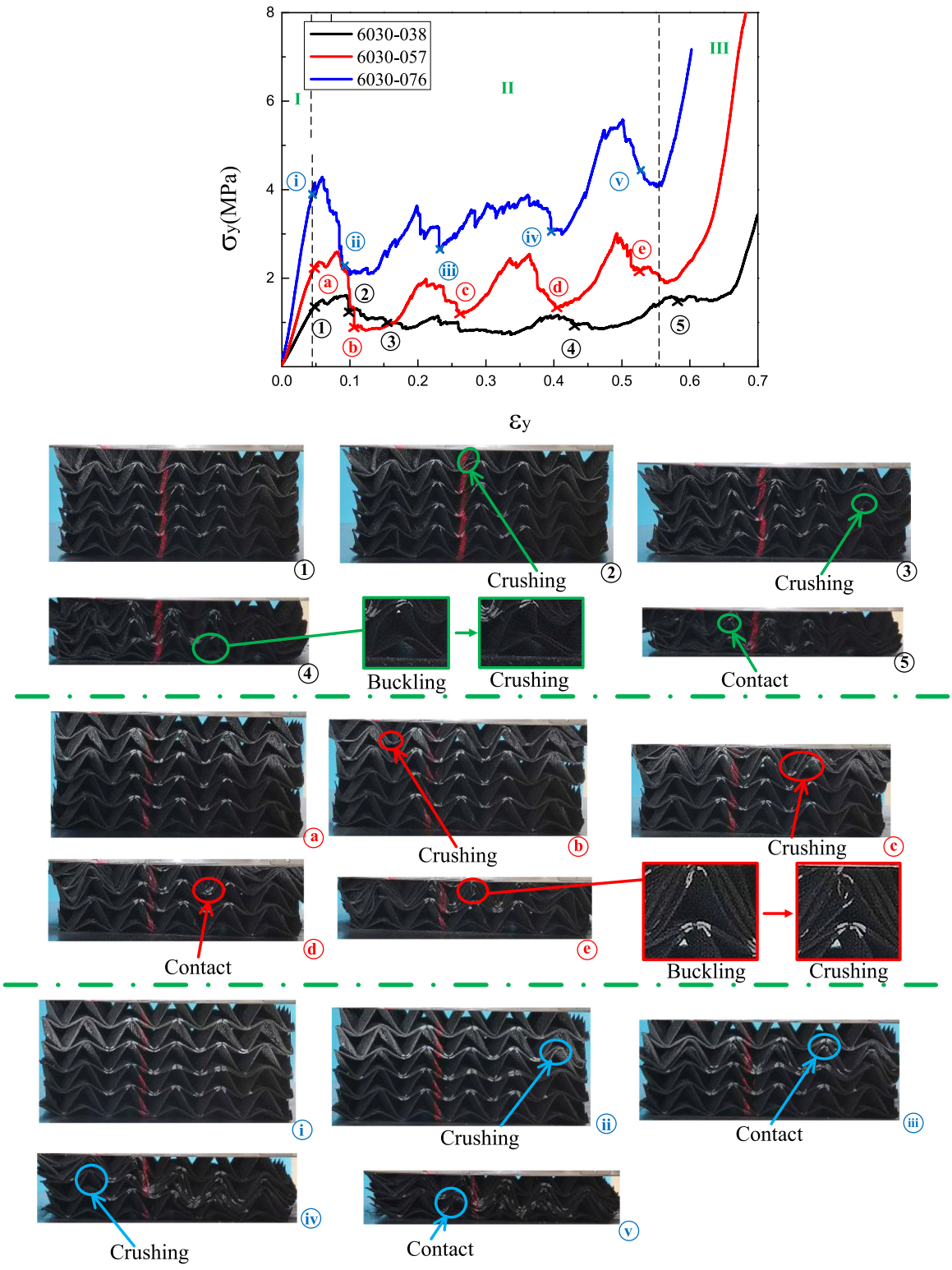

Fig. 12. Failure process of composite origami stack structure with the same parameter $\cos\Psi_A/\cos\Psi_B = 0.58$, and t/l = 0.0475, 0.07125, 0.095, respectively.

to the Ashby's material selection maps. Taking density as variable, different color ellipses are used to wrap the compression stiffness of auxetic structures in different literatures [11,23,46–48]. The specific stiffness of the composite stacked origami structures is superior to those of the Ti6-Al4-V 3D cubic chiral lattice structures and Al corrugated plate-tube auxetic structures having the same densities. The stiffnesses of the composite stacked origami structures are higher than those of the CFRP 3D double-arrow-head structures and CFRP curved-crease origami structures, and the densities of the composite stacked origami structures are higher than those of the CFRP 3D double-arrow-head structures and CFRP curved-crease origami structures.

Comparing the composite stacked origami structures with a variety of structures with energy absorption advantages in the same way [1,41,48–52], it can be found that, compared with the stacked origami structures made of 316L, the density of the stacked origami structures decreases greatly after the base material is replaced with fiber

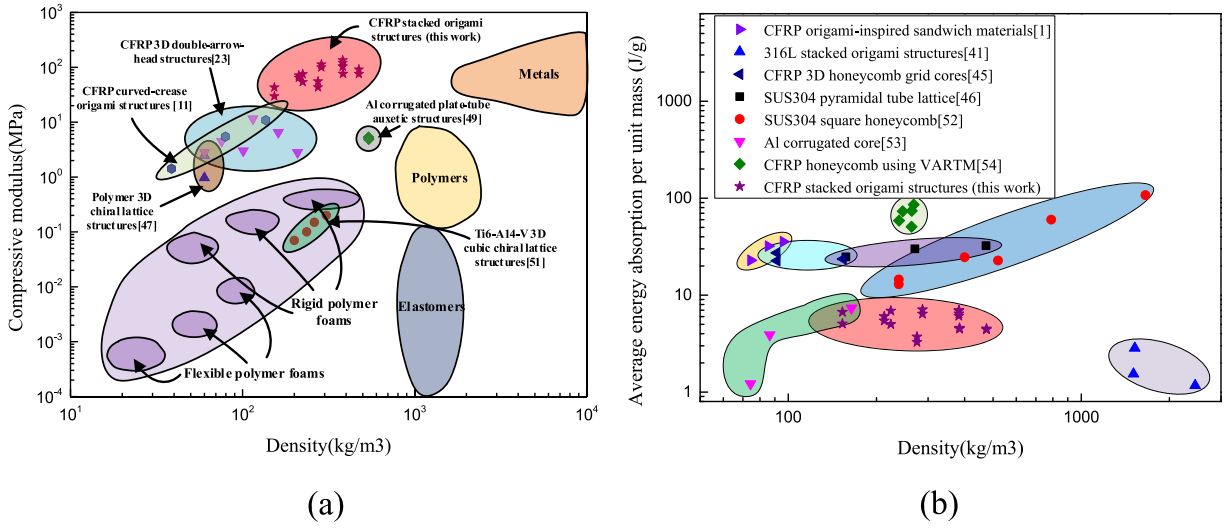

Fig. 13. Modified Ashby material selection maps. (a) Compressive modulus against density, (b) Energy absorption capacity against density.

reinforced composite material, and the energy absorption characteristics of the structure also increases. However, the composite stacked origami structures have not displayed superior energy absorption efficiency as expected compared with other structures. And this is mainly caused by manufacturing defects. Measures should be taken in the future studies to reduce manufacturing defects to fully exploit the compression strength, stiffness and energy absorption efficiency of the composite stacked origami structures.

6. Conclusions

This paper presents the manufacture and characterization of the composite stacked origami structures made from CFRP. The effects of the sheet thickness and the stacking angles on their stiffness, strength, auxetic response, deformation mechanisms, failure modes, and energy absorption capacity under quasi-static compression are studied. And the main conclusions are as follows:

(a) With appropriate geometric parameters and traditional manufacturing methods, high-performance composite origami stacked structures can be mass-produced at a low cost.

(b) Under different compression conditions, the parameters $\cos\Psi_A/\cos\Psi_B$ and t have a decisive influence on the auxetic characteristics of the structure. In out-of-plane compression, the auxetic characteristics of the structure increase with the decrease of parameter $\cos\Psi_A/\cos\Psi_B$. The influence of parameter t on Poisson's ratio is different under different compression conditions. In the process of out-of-plane compression, the influence of thickness t on the structure's Poisson's ratio is very small and can be ignored, while in the process of in-plane compression, the Poisson's ratio v_{zy} is closely related to the thickness t, and the structure's Poisson ratio increases with the increase of thickness t.

(c) The destruction of composite stacked origami structures is mainly composed of four stages, namely the linear elastic stage, buckling, stress platform stage and the densification stage. In the compression process, there will be multiple peaks and troughs, this is mainly related with the layer n. When the structure parameters of t/l and $\cos\Psi_A/\cos\Psi_B$ reach a certain degree, the compression process, the structure of buckling is not obvious.

(d) The specific compressive stiffness of the auxetic structures can be improved by using high performance composite materials. Compared with the stacked origami structures made from metal using additive manufacturing process, composite stacked origami structures have lower density and better energy absorption characteristics.

The composite stacked origami structures studied in this paper is suitable for using in a wide range of industrial fields due to its easier fabrication, superior compressive stiffness, and negative Poisson's ratio characteristics in all directions.

CRediT authorship contribution statement

Zhen-Yu Li: Writing – original draft, Visualization, Validation, Software, Methodology, Investigation, Formal analysis, Data curation. **Xin-Tao Wang:** Writing – review & editing, Validation, Supervision, Resources, Project administration, Conceptualization. **Li Ma:** Writing – review & editing, Validation, Supervision. **Lin-Zhi Wu:** Validation, Supervision, Resources, Project administration. **Lifeng Wang:** Writing – review & editing, Validation, Supervision.

Declaration of competing interest

The authors declare that they have no known competing financial interests or personal relationships that could have appeared to influence the work reported in this paper.

Data availability

No data was used for the research described in the article.

Acknowledgment

This work was supported by the National Natural Science Foundation of China under grant No. 11902095.

References

[1] Y. Du, T. Keller, C. Song, et al., Origami-inspired carbon fiber-reinforced composite sandwich materials – Fabrication and mechanical behavior, Compos. Sci. Technol. (2021) 205.
[2] L. Mahadevan, S. Rica, Self-organized origami, Science 307 (2005) 1740.
[3] J.L. Silverberg, A.A. Evans, L. McLeod, et al., Applied origami, using origami design principles to fold reprogrammable mechanical metamaterials, Science 345 (2014) 647–650.
[4] S. Felton, M. Tolley, E. Demaine, et al., A method for building self-folding machines, Science 345 (2014) 644–646.
[5] M. Schenk, S.D. Guest, Geometry of miura-folded metamaterials, Proc. Natl. Acad. Sci. USA 110 (2013) 3276–3281.
[6] M. Schenk, S.D. Guest, G.J. McShane, Novel stacked folded cores for blast-resistant sandwich beams, Int. J. Solids Struct. 51 (2014) 4196–4214.

[7] Y. Wei, S. Pellegrino, Modular foldable surfaces: a novel approach based on spatial mechanisms and thin shells, in: 4th AIAA Spacecraft Structures Conference, 2017.
[8] X. Xin, L. Liu, Y. Liu, et al., Mechanical models, structures, and applications of shape-memory polymers and their composites, Acta Mech. Solida Sin. 32 (2019) 535–565.
[9] K. Kuribayashi, K. Tsuchiya, Z. You, et al., Selfdeployable origami stent grafts as a biomedical application of Ni-rich TiNi shape memory alloy foil, Mater. Sci. Eng. A 419 (2006) 131–137.
[10] N. Sekularac, J. Ivanovic-Sekularac, J. Cikic-Tovarovic, Folded structures in modern architecture, Facta Univ. Ser.: Archit. Civ. Eng. 10 (2012) 1–16.
[11] Y. Du, C. Song, J. Xiong, et al., Fabrication and mechanical behaviors of carbon fiber reinforced composite foldcore based on curved-crease origami, Compos. Sci. Technol. 174 (2019) 94–105.
[12] W. Li, Q. Zheng, H. Fan, et al., Fabrication and mechanical testing of ultralight folded lattice-core sandwich cylinders, Engineering 6 (2020) 196–204.
[13] B. Liu, Y. Sun, Y. Sun, et al., Fabrication and compressive behavior of carbon-fiber-reinforced cylindrical foldcore sandwich structure, Composites A 118 (2019) 9–19.
[14] J.A. Harris, G.J. McShane, Impact response of metallic stacked origami cellular materials, Int. J. Impact Eng. 147 (2021).
[15] B. Liu, Y. Sun, Modal response of carbon-fiber-reinforced miura-ori core sandwich panels, Mech. Adv. Mater. Struct. 27 (2018) 364–372.
[16] X. Wei, J. Xiong, J. Wang, et al., New advances in fiber-reinforced composite honeycomb materials, Sci. Chin. Technol. Sci. 63 (2020) 1348–1370.
[17] Y. Klett, P. Middendorf, W. Sobek, et al., Potential of origami-based shell elements as next-generation envelope components, in: 2017 IEEE International Conference on Advanced Intelligent Mechatronics (AIM), 2017.
[18] Y. Du, T. Keller, C. Song, et al., Design and foldability of Miura-based cylindrical origami structures, Thin-Walled Struct. (2021) 159.
[19] J.M. Gattas, Z. You, The behaviour of curved-crease foldcores under low-velocity impact loads, Int. J. Solids Struct. 53 (2015) 80–91.
[20] Y. Lv, Y. Zhang, N. Gong, et al., On the out-of-plane compression of a Miura-ori patterned sheet, Int. J. Mech. Sci. (2019) 161–162.
[21] L. Yuan, H. Dai, J. Song, et al., The behavior of a functionally graded origami structure subjected to quasi-static compression, Mater. Des. (2020) 189.
[22] D.Y. Seong, C.G. Jung, D.Y. Yang, et al., Quasi-isotropic bending responses of metallic sandwich plates with bi-directionally corrugated cores, Mater. Des. 31 (2010) 2804–2812.
[23] X.T. Wang, B. Wang, Z.H. Wen, et al., Fabrication and mechanical properties of CFRP composite three-dimensional double-arrow-head auxetic structures, Compos. Sci. Technol. 164 (2018) 92–102.
[24] S. Heimbs, P. Middendorf, S. Kilchert, et al., Experimental and numerical analysis of composite folded sandwich core structures under compression, Appl. Compos. Mater. 14 (2008) 363–377.
[25] S. Heimbs, J. Cichosz, M. Klaus, et al., Sandwich structures with textile-reinforced composite foldcores under impact loads, Compos. Struct. 92 (2010) 1485–1497.
[26] Y. Sun, Y. Li, Prediction and experiment on the compressive property of the sandwich structure with a chevron carbon-fibre-reinforced composite folded core, Compos. Sci. Technol. 150 (2017) 95–101.
[27] A.A. Deleo, J. O'Neil, H. Yasuda, et al., Origami-based deployable structures made of carbon fiber reinforced polymer composites, Compos. Sci. Technol. (2020) 191.
[28] S. Li, J.S. Yang, S.Y. Chen, et al., Modal response and vibration attenuation of carbon fiber composite sandwich cylindrical panels made of bi-directional corrugated strip cores, Mech. Adv. Mater. Struct. (2020) 1–15.
[29] S. Li, J.S. Yang, L.Z. Wu, et al., Vibration behavior of metallic sandwich panels with Hourglass truss cores, Mar. Struct. 63 (2019) 84–98.
[30] J.S. Yang, Z.D. Liu, R. Schmidt, et al., Vibration-based damage diagnosis of composite sandwich panels with bi-directional corrugated lattice cores, Composites A (2020) 131.
[31] J.S. Yang, L. Ma, M. Chaves-Vargas, et al., Influence of manufacturing defects on modal properties of composite pyramidal truss-like core sandwich cylindrical panels, Compos. Sci. Technol. 147 (2017) 89–99.
[32] J.S. Yang, J. Xiong, L. Ma, et al., Modal response of all-composite corrugated sandwich cylindrical shells, Compos. Sci. Technol. 115 (2015) 9–20.
[33] A. Alomarah, J. Zhang, D. Ruan, et al., Mechanical properties of the 2D re-entrant honeycomb made via direct metal printing, IOP Conf. Ser.: Mater. Sci. Eng. (2017) 229.
[34] Y. Gao, Q. Wu, X. Wei, et al., Composite tree-like re-entrant structure with high stiffness and controllable elastic anisotropy, Int. J. Solids Struct. 206 (2020) 170–182.
[35] X.T. Wang, Y.L. Chen, L. Ma, The manufacture and characterization of composite three-dimensional re-entrant auxetic cellular structures made from carbon fiber reinforced polymer, J. Compos. Mater. 52 (2018) 3265–3273.
[36] X.T. Wang, B. Wang, X.W. Li, et al., Mechanical properties of 3D re-entrant auxetic cellular structures, Int. J. Mech. Sci. 131–132 (2017) 396–407.
[37] L. Yang, O. Harrysson, H. West, et al., Mechanical properties of 3D re-entrant honeycomb auxetic structures realized via additive manufacturing, Int. J. Solids Struct. 69–70 (2015) 475–490.
[38] Y.L. Chen, X.T. Wang, L. Ma, Damping mechanisms of CFRP three-dimensional double-arrow-head auxetic metamaterials, Polym. Test. 164 (2020) 92–102.
[39] X. Zhao, Q. Gao, L. Wang, et al., Dynamic crushing of double-arrowed auxetic structure under impact loading, Mater. Des. 160 (2018) 527–537.
[40] Z.Y. Li, X.T. Wang, J.S. Yang, et al., Mechanical response and auxetic properties of composite double arrow corrugated sandwich panels with defects, Mech. Adv. Mater. Struct. (2021).
[41] J.A. Harris, G.J. McShane, Metallic stacked origami cellular materials: Additive manufacturing, properties, and modelling, Int. J. Solids Struct. 185–186 (2020) 448–466.
[42] Z.Y. Li, X.T. Wang, L. Ma, et al., Study on the mechanical properties of CFRP composite auxetic structures consist of corrugated sheets and tubes, Compos. Struct. 292 (2022) 115655.
[43] S. Li, J.S. Yang, R. Schmidt, et al., Compression and hysteresis responses of multilayer gradient composite lattice sandwich panels, Mar. Struct. (2021) 75.
[44] J. Xiong, A. Vaziri, R. Ghosh, et al., Compression behavior and energy absorption of carbon fiber reinforced composite sandwich panels made of three-dimensional honeycomb grid cores, Extreme Mech. Lett. 7 (2016) 114–120.
[45] B. Hu, L.Z. Wu, J. Xiong, et al., Mechanical properties of a node-interlocking pyramidal welded tube lattice sandwich structure, Mech. Mater. 129 (2019) 290–305.
[46] M. Fu, F. Liu, L. Hu, A novel category of 3D chiral material with negative Poisson's ratio, Compos. Sci. Technol. 160 (2018) 111–118.
[47] Z. Zhang, H. Hu, S. Liu, et al., Study of an auxetic structure made of tubes and corrugated sheets, Phys. Status Solidi (B) (2013) 1–6.
[48] F. Warmuth, F. Osmanlic, L. Adler, et al., Fabrication and characterisation of a fully auxetic 3D lattice structure via selective electron beam melting, Smart Mater. Struct. (2017) 26.
[49] X.T. Wang, X.W. Li, L. Ma, Interlocking assembled 3D auxetic cellular structures, Mater. Des. 99 (2016) 467–476.
[50] F. Côté, V.S. Deshpande, N.A. Fleck, et al., The compressive and shear responses of corrugated and diamond lattice materials, Int. J. Solids Struct. 43 (2006) 6220–6242.
[51] B. Han, K. Qin, B. Yu, et al., Honeycomb–corrugation hybrid as a novel sandwich core for significantly enhanced compressive performance, Mater. Des. 93 (2016) 271–282.
[52] R.A. Alia, O. Al-Ali, S. Kumar, et al., The energy-absorbing characteristics of carbon fiber-reinforced epoxy honeycomb structures, J. Compos. Mater. 53 (2018) 1145–1157.